The Astrophysical Journal, 981:120 (11pp), 2025 March 10 https://doi.org/10.3847/1538-4357/adb0b5

Unusual X-Ray Oxygen Line Ratios of SN 1987A Arising from the Absorption of Galactic Hot Interstellar Medium

Lei Sun[1,2,3], Salvatore Orlando[4], Emanuele Greco[3,4,5], Marco Miceli[4,5], Yiping Li[1], Yang Chen[1,2], Jacco Vink[3], and Ping Zhou[1,2]

[1] Department of Astronomy, Nanjing University, Nanjing 210023, People's Republic of China; l.sun@nju.edu.cn
[2] Key Laboratory of Modern Astronomy and Astrophysics, Nanjing University, Ministry of Education, People's Republic of China
[3] Anton Pannekoek Institute & GRAPPA, University of Amsterdam, PO Box 94249, 1090 GE Amsterdam, The Netherlands
[4] INAF—Osservatorio Astronomico di Palermo, Piazza del Parlamento 1, 90134 Palermo, Italy
[5] Dipartimento di Fisica e Chimica "E. Segrè",Università degli Studi di Palermo, Piazza del Parlamento 1, 90134 Palermo, Italy
Received 2024 August 14; revised 2025 January 19; accepted 2025 January 29; published 2025 March 4

Abstract

Recent high-resolution X-ray spectroscopic studies have revealed unusual oxygen line ratios, such as the high O VII forbidden-to-resonance ratio, in several supernova remnants. While the physical origin is still under debate, for most of them it has been suggested that this phenomenon arises from either charge exchange (CX) or resonant scattering (RS). In this work, we report the high O VII G-ratio ($\gtrsim$1) and high O VIII Lyβ/Lyα ratio ($\gtrsim$0.2) found in multiepoch XMM-Newton Reflection Grating Spectrometer observations of SN 1987A. The line ratios cannot be fully explained by nonequilibrium ionization effects, CX, or RS. We suggest the absorption of foreground hot gas as the most likely origin, which plays the major role in modifying line fluxes and line ratios. Based on this scenario, we introduced two Gaussian absorption components at the O VII resonance line and the O VIII Lyα line and constrained the optical depth of the two lines as $\tau_{\rm O\ VII} \sim 0.6$ and $\tau_{\rm O\ VIII} \sim 0.2$. We estimated the temperature as $kT_{\rm e} \sim 0.15$ keV and the oxygen column density as $N_{\rm O} \sim 0.5 \times 10^{16}$ cm^{-2} for the absorbing gas, which is consistent with the hot interstellar medium in the Galactic halo. Neglecting this absorption component may lead to an underestimation of the O abundance. We revised the O abundance of SN 1987A, which is increased by ~20% compared with previous results. The N/O ratio by number of atoms is revised to be ~1.2.

Unified Astronomy Thesaurus concepts: X-ray astronomy (1810); Supernova remnants (1667); Interstellar medium (847)

1. Introduction

High-resolution X-ray spectroscopy of supernova remnants (SNRs) has provided us with profound insights into the radiation mechanisms and chemical compositions of the shocked ejecta, circumstellar material (CSM), and interstellar medium (ISM), significantly advancing our understanding of shock physics, progenitor type, explosion mechanism, and remnant evolution (see, e.g., S. Katsuda 2023 for a recent review). Particularly, the emission line ratios of He-like and H-like ions, such as the O VII G-ratio and the O VIII Lyβ/Lyα ratio, play an important role in the diagnostics of the temperature and ionization age of hot plasmas (e.g., D. Porquet et al. 2010). However, due to the complex nature of SNRs, these line ratios can be affected by different physical processes.

Recently, unusually high O VII G-ratios (or forbidden-to-resonance line ratios) have been found in several SNRs, such as the Cygnus Loop (S. Katsuda et al. 2011; S. R. Roberts & Q. D. Wang 2015; H. Uchida et al. 2019), Puppis A (S. Katsuda et al. 2012), N49 (Y. Amano et al. 2020), N132D (H. Suzuki et al. 2020), G296.1−0.5 (Y. Tanaka et al. 2022), and J0453.6−6829 (Y. Koshiba et al. 2022). While the physical origin is still under debate, two major alternative scenarios have been proposed, namely either charge exchange (CX) or resonant scattering (RS).

In the CX process, an electron is transferred from one atom or ion to another. The newly captured electron will cascade from a highly excited state to the ground level and result in a series of emission lines. CX will boost the forbidden line of the He-like triplet, thus leading to a large G-ratio (e.g., R. K. Smith et al. 2012; L. Gu et al. 2016; L. Gu & C. Shah 2023). On the other hand, RS will change the directions of the resonance photons, which may suppress the observed resonance line flux in some circumstances, depending on the geometry, and result in a large G-ratio (e.g., Y. Li et al. 2024).

One of the other possible scenarios is the resonant absorption of the foreground hot gas, which has not yet been investigated in detail in the context of SNRs. A hot ISM component with a temperature as high as ~0.15–0.22 keV has been found in the Galactic halo based on its X-ray emission (e.g., D. B. Henley & R. L. Shelton 2013; M. Ueda et al. 2022; G. Ponti et al. 2023). The absorption features left by this hot Galactic ISM, such as the O VII and O VIII absorption lines, have also been detected in the X-ray spectra of several Galactic and Magellanic X-ray binaries (e.g., Q. D. Wang et al. 2005; Y. Yao et al. 2008; Y. Luo et al. 2018). Therefore, it is very likely that the observed O line fluxes of SNRs, especially Magellanic SNRs, are affected by this absorption component in the same way.

The study of O line ratios can help us to further explore the role that CX, RS, and hot gas absorption play in the X-ray spectral properties of SNRs. More importantly, if these effects have not been properly considered in the X-ray analysis, the measured metal abundances of the shocked ejecta/CSM/ISM may be distorted, and thus any further discussions based on that may be questioned.

Located in the Large Magellanic Cloud (LMC), SN 1987A is the nearest supernova (SN) observed since Kepler's SN of 1604. It was a Type II explosion of a blue supergiant. The peculiar CSM system of SN 1987A consists of three coaxial rings—one equatorial ring (ER) and two side rings constituting an hourglass-like structure. The SN blast wave encountered the innermost layer of the ER at ∼4000 days after the explosion, as indicated by the brightening of several "hot spots" in the optical band and the corresponding excess of the soft X-ray flux (e.g., G. Sonneborn et al. 1998; D. N. Burrows et al. 2000; S. S. Lawrence et al. 2000; S. Park et al. 2002). Soon after, the front shock reached the main body of the ER at ∼6000 days, and has been heavily interacting with it since then (e.g., S. Park et al. 2005; J. L. Racusin et al. 2009; E. A. Helder et al. 2013; K. A. Frank et al. 2016), making SN 1987A one of the youngest and brightest SNRs. The X-ray emission of SN 1987A is now dominated by the shock-heated plasma within the ER, including dense clumps and interclump materials, with a density $\sim 10^3$–$10^4\,\mathrm{cm}^{-3}$. On the other hand, the shocked low-density H II region ($\sim 10^2\,\mathrm{cm}^{-3}$), high-latitude materials beyond the ER, and the outermost-layer ejecta also make significant contributions (e.g., D. Dewey et al. 2012; S. Orlando et al. 2020; L. Sun et al. 2021; A. P. Ravi et al. 2024; L. Sun et al. 2025). The small angular size (∼2″; e.g., J. L. Racusin et al. 2009) and high X-ray brightness ($\sim 7.8 \times 10^{-12}\,\mathrm{erg\,cm^{-2}\,s^{-1}}$ in 0.5–2.0 keV; e.g., L. Sun et al. 2021) of SN 1987A enable high-resolution X-ray spectroscopic studies using X-ray grating spectrometers, which have yielded fruitful results regarding the structure and evolution of the remnant, the physical properties of the shocked ejecta and CSM, the collisionless shock-heating mechanism, and so on (e.g., S. A. Zhekov et al. 2009; R. Sturm et al. 2010; D. Dewey et al. 2012; M. Miceli et al. 2019; L. Sun et al. 2021). This also makes SN 1987A an excellent target in studies of CX, RS, and hot gas absorption in SNRs.

Such studies rely on a comprehensive understanding of the physical properties of the thermally emitting gas. Due to the complex structure of the remnant, the shock-heated plasmas in SN 1987A span a wide range of physical conditions (e.g., temperatures and ionization parameters), which have been extensively revealed by previous studies via X-ray spectral analysis (e.g., S. Park et al. 2004, 2006; F. Haberl et al. 2006; S. A. Zhekov et al. 2006, 2009, 2010; K. Heng et al. 2008; R. Sturm et al. 2010; D. Dewey et al. 2012; K. A. Frank et al. 2016; E. Bray et al. 2020; D. Alp et al. 2021; E. Greco et al. 2021, 2022; A. P. Ravi et al. 2021, 2024; L. Sun et al. 2021; C. Maitra et al. 2022). As summarized by D. Alp et al. (2021, see Table 6 therein), these works found plasma temperatures in the range of ∼0.5–4 keV, with a low-temperature component at ∼0.5 keV dominated by the dense ER, a high-temperature component at ∼2–4 keV dominated by the H II region and the outermost ejecta, and in some of them a third intermediate-temperature component at ∼1 keV. The ionization parameters of the plasmas, on the other hand, also span a wide range from $\sim 10^{10}$–$10^{13}\,\mathrm{cm}^{-3}\,\mathrm{s}$. Recently, L. Sun et al. (2025) obtained the continuous temperature distributions of SN 1987A by fitting the Reflection Grating Spectrometer (RGS) plus EPIC-pn spectra with a differential emission measure (DEM) model. The obtained temperature distributions reveal a major peak at ∼0.6–1 keV with a high-temperature tail extending to $\gtrsim$5 keV, well consistent with the magnetohydrodynamic simulations by S. Orlando et al. (2020), which help to reveal the fading of the ER and the brightening of the shocked ejecta. Their results provided one of the most accurate depictions of the X-ray emission of SN 1987A, but still far from perfect. Since the DEM model considered only the thermal emission from the non-equilibrium ionization (NEI) plasmas, it is still worthwhile to take a further look into the residuals that may provide information about other mechanisms such as CX, RS, and hot gas absorption.

In this work, we extend the discussions in L. Sun et al. (2025) by examining the residuals left by the DEM modeling at O lines. We describe the observations and the reduction procedures in Section 2, revise and update the O line fluxes and line ratios in Section 3, explore the physical origin of the unusual O line ratios in Section 4, and finally make our conclusions in Section 5.

2. Observations and Data Reduction

We utilized the same data set adopted in L. Sun et al. (2025), which contains XMM-Newton observations collected in 14 epochs from 2007 to 2021. All the data were processed using the XMM-Newton Science Analysis Software (SAS, v18.0.0) with the latest calibration files.[6] We extracted the EPIC-pn and RGS spectra following L. Sun et al. (2021). The spectra were then optimally rebinned, adopting the J. S. Kaastra & J. A. M. Bleeker (2016) optimal binning scheme. Due to the small angular size, SN 1987A cannot be spatially resolved by XMM-Newton, and thus was treated as a point-like source. Thereby, the extracted spectra represent the integrated X-ray emission from the whole remnant, and the RGS spectral resolution (∼2 eV at ∼0.6 keV for O lines) will not be affected by the source extent.

Unless otherwise specified, in this paper the metal abundances are presented with respect to their solar values (J. Wilms et al. 2000), and the error bars represent the 1σ uncertainties.

3. Oxygen Line Ratios

The X-ray spectra of SN 1987A have been extensively analyzed based on different observations with different spectral models (e.g., S. A. Zhekov et al. 2009; M. Miceli et al. 2010; D. Dewey et al. 2012; D. Alp et al. 2021; A. P. Ravi et al. 2021; L. Sun et al. 2021; C. Maitra et al. 2022). Recently, L. Sun et al. (2025) successfully fitted the X-ray spectra of SN 1987A using a DEM model and provided significantly improved results (fit statistics) compared with the previous discrete models (e.g., a two-temperature model as in L. Sun et al. 2021). With the DEM model, L. Sun et al. (2025) characterized the continuous distribution of the X-ray gas in SN 1987A in a temperature range of 0.1–10 keV. They assumed a power-law relation between the ionization parameter and the plasma temperature, and an identical metal abundance among different temperature components. Their results revealed a major peak in the DEM distribution at ∼0.5–1 keV, with a high-temperature tail extending to $\gtrsim$5 keV. Here, we adopted their best-fit models and compared them with the RGS spectra of SN 1987A. We found that the DEM models still leave some residuals in the fitted spectra. The most prominent residual features are lying in the O VII triplets and the O VIII Lyα lines, where the model overestimated the O VII resonance line and the O VIII Lyα lines while underestimating the O VII forbidden line (Figure 1).

[6] https://www.cosmos.esa.int/web/xmm-newton/sas

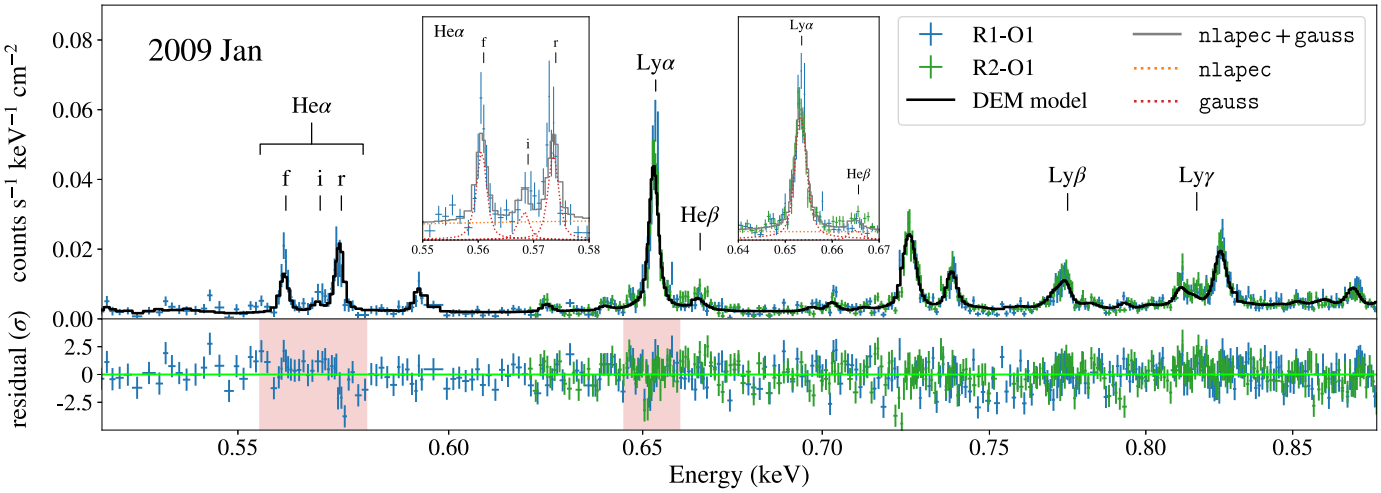

Figure 1. An example of the O-emitting band spectra of SN 1987A fitted with the DEM model (L. Sun et al. 2025). The major O lines are labeled. The red boxes highlight the major residuals left in the DEM modeling, where the model overestimated the O VII resonance line and the O VIII Lyα lines while underestimating the O VII forbidden line. The two subplots show a zoomed-in view of O VII Heα and O VIII Lyα, fitted with the "`nlapec + Gauss`" model.

Table 1
Oxygen Line Fluxes and Ratios of SN 1987A

Obs. Date	Age (Days)	Line Flux (10^{-5} photon cm^{-2} s^{-1})					Line Ratio	
		O VII f (0.5611 keV)	O VII i (0.5686 keV)	O VII r (0.5740 keV)	O VIII Lyα (0.6537 keV)	O VIII Lyβ (0.7746 keV)	G-ratio	Lyβ/Lyα
2007 Jan 17	7267	$12.64^{+1.51}_{-2.18}$	$1.26^{+3.05}_{-0.93}$	$14.91^{+1.87}_{-1.89}$	$34.47^{+1.03}_{-0.80}$	$6.88^{+0.68}_{-0.42}$	$0.93^{+0.26}_{-0.20}$	$0.20^{+0.02}_{-0.01}$
2008 Jan 11	7627	$15.06^{+2.35}_{-2.89}$	$4.28^{+2.45}_{-1.68}$	$18.03^{+3.41}_{-3.19}$	$43.24^{+2.20}_{-2.47}$	$7.76^{+0.37}_{-0.43}$	1.07 ± 0.27	0.18 ± 0.01
2009 Jan 30	8012	$18.07^{+1.08}_{-1.41}$	$5.81^{+1.94}_{-2.89}$	$14.32^{+2.69}_{-1.72}$	$45.63^{+0.81}_{-1.85}$	$10.07^{+0.63}_{-0.56}$	$1.67^{+0.25}_{-0.39}$	$0.22^{+0.02}_{-0.01}$
2009 Dec 11	8327	$13.65^{+2.08}_{-1.73}$	$3.66^{+1.14}_{-0.59}$	$14.09^{+1.36}_{-2.13}$	$49.01^{+2.90}_{-1.37}$	$10.20^{+0.42}_{-1.07}$	$1.23^{+0.25}_{-0.18}$	$0.21^{+0.01}_{-0.03}$
2010 Dec 12	8693	$16.69^{+3.02}_{-0.99}$	$0.32^{+2.69}_{-0.24}$	$14.26^{+2.30}_{-3.18}$	$52.22^{+0.50}_{-1.48}$	$11.49^{+1.28}_{-0.76}$	$1.19^{+0.39}_{-0.21}$	$0.22^{+0.03}_{-0.01}$
2011 Dec 2	9048	$14.08^{+2.31}_{-2.92}$	$4.23^{+1.15}_{-2.62}$	$12.32^{+4.16}_{-1.47}$	$51.07^{+1.37}_{-2.27}$	$12.37^{+0.78}_{-0.57}$	$1.49^{+0.27}_{-0.59}$	$0.24^{+0.02}_{-0.01}$
2012 Dec 11	9423	$14.00^{+2.79}_{-1.22}$	<3.28	$11.09^{+3.00}_{-1.86}$	$48.57^{+1.15}_{-0.41}$	$12.09^{+0.58}_{-0.69}$	$1.26^{+0.44}_{-0.36}$	$0.25^{+0.01}_{-0.02}$
2014 Nov 29	10141	$7.61^{+2.02}_{-1.81}$	$6.95^{+2.48}_{-1.55}$	$13.88^{+2.86}_{-3.37}$	$37.28^{+0.78}_{-1.02}$	$9.31^{+0.92}_{-0.83}$	$1.05^{+0.58}_{-0.28}$	$0.25^{+0.03}_{-0.02}$
2015 Nov 15	10492	$1.75^{+2.70}_{-1.31}$	$5.60^{+2.85}_{-1.90}$	$8.87^{+1.73}_{-1.05}$	$35.75^{+1.35}_{-1.18}$	$7.14^{+0.78}_{-1.07}$	$0.83^{+0.71}_{-0.31}$	$0.20^{+0.02}_{-0.03}$
2016 Nov 2	10845	$5.69^{+1.83}_{-1.32}$	$1.42^{+1.50}_{-1.07}$	$10.66^{+2.15}_{-2.39}$	$37.22^{+0.92}_{-1.47}$	$8.03^{+1.14}_{-0.66}$	$0.67^{+0.26}_{-0.21}$	$0.22^{+0.03}_{-0.02}$
2017 Oct 15	11192	$7.57^{+2.50}_{-2.56}$	$3.41^{+1.60}_{-2.16}$	$7.93^{+2.16}_{-1.32}$	$28.93^{+1.47}_{-1.39}$	$7.84^{+0.52}_{-0.78}$	$1.38^{+0.58}_{-0.57}$	$0.27^{+0.02}_{-0.03}$
2019 Nov 27	11964	<0.22	$5.19^{+1.66}_{-0.76}$	$4.73^{+0.42}_{-0.44}$	$25.87^{+0.30}_{-0.24}$	$7.05^{+0.73}_{-0.94}$	$1.10^{+1.10}_{-0.19}$	$0.27^{+0.03}_{-0.04}$
2020 Nov 24	12328	<2.86	$5.62^{+3.41}_{-3.23}$	$7.48^{+3.28}_{-3.12}$	$30.71^{+1.82}_{-1.69}$	$6.55^{+1.32}_{-1.38}$	$0.79^{+0.66}_{-0.55}$	$0.21^{+0.04}_{-0.05}$
2021 Dec 28	12727	$3.49^{+1.96}_{-2.01}$	<1.48	<3.33	22.68 ± 1.51	$4.22^{+0.90}_{-0.87}$	...	0.19 ± 0.04

L. Sun et al. (2021) measured the fluxes of 36 emission lines in the X-ray spectra of SN 1987A and followed their evolution from 2007 to 2019 by fitting the RGS spectra with a model containing one continuum (described by the `nlapec` model, which includes the thermal bremsstrahlung, the radiative recombination continua, and the two-photon emission) plus multiple Gaussian lines (described by several `Gauss` components).[7] Here, we revised and updated their results by applying the same procedure to the updated data set, which contains two additional observations taken in 2020 and 2021. We measured the fluxes of the most prominent O lines (i.e., the forbidden, intercombination, and resonance lines for O VII, and the Lyα and Lyβ lines for O VIII). Based on these updated line fluxes, we calculated the O VII G-ratio (defined as $\mathcal{G} \equiv (F + I)/R$, where F, I, and R stand for the flux of the forbidden, intercombination, and resonance lines, respectively) and the O VIII Lyβ/Lyα ratio for SN 1987A from 2007 to 2021. The line fluxes and ratios are summarized in Table 1. Given the complex structure of SN 1987A (as described in Section 1), one should keep in mind that different components of the remnant, such as the shocked ER, H II region, high-latitude materials, and outer-layer ejecta, contribute to the O lines simultaneously. Thereby, the O line fluxes and ratios measured here represent the average properties of all these components with a large range of physical conditions.

For collisional ionization equilibrium (CIE) or NEI (under-ionized) plasma, the O VII G-ratio is commonly in the range of $\sim$0.5–1, varying with temperature and ionization parameter, while O VIII Lyβ/Lyα is commonly in the range of $\sim$0–0.15, varying with temperature (e.g., R. Mewe 1999; J. S. Kaastra et al. 2008; D. Porquet et al. 2010, and see the discussions in Section 4.1). However, according to the above results, we found a high O VII G-ratio $\gtrsim$1 and a high O VIII Lyβ to Lyα ratio $\gtrsim$0.2 in SN 1987A, especially in the epoch from 2009 to 2012 when the O lines were around their maximum luminosity (Figure 2).

[7] https://heasarc.gsfc.nasa.gov/xanadu/xspec/manual/XSmodelNlapec.html

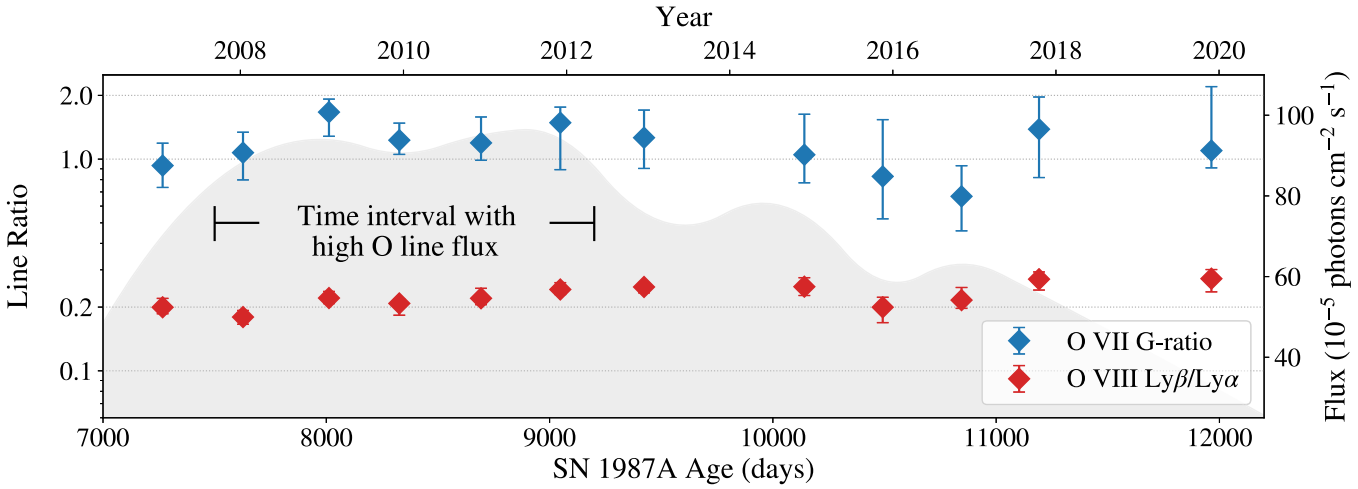

Figure 2. O line ratios and their temporal evolutions in SN 1987A. The blue and red data points denote the O VII G-ratio and the O VIII Lyβ/Lyα flux ratio, respectively. The gray underfilled curve indicates the temporal evolution of the total O line flux (O VII Heα + O VIII Lyα).

We note that the measured O VIII Lyβ flux may be affected by Fe L lines, such as the contribution from the Fe XVIII F6 line ($2s^22p^43s^2P_{3/2} \rightarrow 2s^22p^{52}P_{3/2}$ at 0.775 keV, line label adopted from G. V. Brown et al. 1998), which may lead to an overestimated O VIII Lyβ/Lyα ratio. The soft-band X-ray emission in SN 1987A is dominated by a low-temperature plasma component with $kT_e \sim 0.6$ keV and $n_et \sim 10^{11}$ cm^{-3} s, according to previous studies (e.g., R. Sturm et al. 2010; D. Alp et al. 2021; A. P. Ravi et al. 2021; C. Maitra et al. 2022). Under this condition, we calculated the emissivities of O VIII Lyβ and Fe XVIII F6, and found the relative contribution of the Fe XVIII F6 line ($\epsilon_{F6}/(\epsilon_{F6} + \epsilon_{Ly\beta})$) to be ~17%. Nevertheless, the O and Fe L emission could be contributed by plasma that spans a larger range of temperatures and ionization parameters, as shown in L. Sun et al. (2025). We then explored a larger parameter space, where the temperature varies between 0.3 and 3 keV and the ionization parameter varies between 10^{11} to 10^{12} cm^{-3} s. The obtained emissivity-weighted average contribution of the Fe XVIII F6 line is ~25%. As a result, we believe the O VIII Lyβ/Lyα ratio measured above might be overestimated by a factor of ~0.3 due to the potential contribution of Fe XVIII F6. However, even after correcting this effect, the O VIII Lyβ/Lyα will still be $\gtrsim$0.15, which is difficult to fully explain with the common CIE/NEI plasma models (see the discussions in Section 4.1).

4. Physical Origin of the Unusual O Line Ratios

As mentioned in the introduction, a high O VII G-ratio has been observed in several SNRs. Despite efforts to understand its origin, it remains unclear whether the primary mechanism responsible is NEI effects, CX processes, RS, or absorption by foreground hot gas. We discuss these possibilities below.

4.1. NEI Effects

The NEI effects of plasmas may either enhance (e.g., at the early stage of ionization when the inner-shell ionization of Li-like ions is boosted due to a large population of Li-like ions, which enhances the forbidden lines) or suppress (e.g., during the ionizing process when populations of Li-like and H-like ions are both low, and thus the inner-shell ionization and the recombination processes are quenched, which suppresses the forbidden lines) the G-ratio of He-like ions compared with that in the CIE scenario (see, e.g., D. Porquet et al. 2010, for a detailed review). For SN 1987A, it is clear that the majority of X-ray plasma is in the NEI state, i.e., still ionizing (e.g., R. Sturm et al. 2010; L. Sun et al. 2021). However, even though previous studies such as L. Sun et al. (2025) have used NEI plasma models for spectral fitting, it is still possible that these models fail to reproduce the line ratios due to the limited model setup and simplified parameter configurations. Therefore, we first explored the possibility of reproducing the observed O VII G-ratios within the NEI regime.

We evaluated the O VII G-ratio in a large kT_e–n_et space, as illustrated by Figure 3 (the calculations were performed using SPEX v3.07.03).[8] We found that the observed O VII G-ratio in SN 1987A can only be reproduced in extreme conditions, i.e., at a very low temperature ($kT_e \lesssim 0.1$ keV) or at the very early ionization stage ($n_et \sim 10^9$ cm^{-3} s). However, at a very low temperature, even though the high G-ratio can be achieved, the O VII lines are rather faint (<1% of their maximum flux). Thereby, the contributions of these low-temperature plasmas can be ignored. On the other hand, since the average density of SN 1987A is pretty high ($\gtrsim 10^3$ cm^{-3}; e.g., L. Sun et al. 2021), the plasma will quickly go through the $n_et \sim 10^9$ cm^{-3} s stage, and move into $n_et \sim 10^{10-12}$ cm^{-3} s. Thus, the contributions of these low-n_et plasmas are also negligible.

In a word, the observed O VII G-ratio cannot be fully explained under the NEI regime. This can be further demonstrated by taking other line ratios into consideration. As shown in Figure 4, by plotting the observed Lyα/Heα ratio together with the G-ratio in the kT_e–n_et diagram, we found that the two line ratios are not consistent with each other—there is no [kT_e, n_et] combination that can reproduce both the O VII G-ratio and the Lyα/Heα ratio simultaneously. However, this inconsistency is only seen for O, while for Ne and Mg the two ratios provide reasonable estimations for the plasma temperature and ionization parameter as $kT_e \sim$ 0.4–1 keV and $n_et \sim 10^{11}$–10^{12} cm^{-3} s. These are comparable with previous results, such as the low-temperature (~0.4 keV) and middle-temperature (~0.8 keV) components of the three-temperature (3-T) `vnei` modeling in E. Greco et al. (2022), representing the X-ray emission dominated by the shocked ER.

[8] https://www.sron.nl/astrophysics-spex/

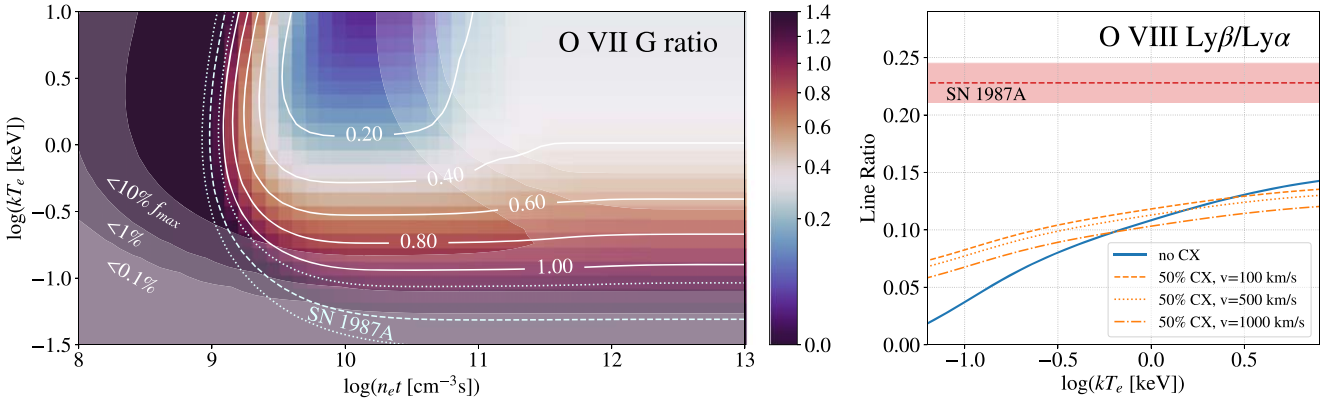

Figure 3. Left: O VII G-ratio as a function of kT_e and $n_e t$ for ionizing NEI plasma. The observed G-ratio for SN 1987A is indicated by the cyan contours, where the dashed line denotes the average value and the dotted lines indicate the error range. The shaded contour regions indicate the levels of total O VII Heα flux as <10%, <1%, and <0.1% of the maximum flux, respectively. Right: O VIII Lyβ/Lyα ratio as a function of kT_e, for both NEI and CIE plasma (NEI effects have little impact on the Lyβ/Lyα ratio, which is similar to that in the CIE scenario). The blue solid line denotes no CX contribution, while the dashed, dotted, and dashed–dotted orange lines denote 50% CX contribution with a collision velocity of 100 km s^{-1}, 500 km s^{-1}, and 1000 km s^{-1}, respectively. The observed flux ratio for SN 1987A is indicated by the red region.

Overionized (recombining) plasma may also lead to enhanced G-ratios. However, this is unlikely to be the case for SN 1987A, since no other recombination features (such as radiative recombination continua) have been observed.

NEI effects have little impact on the Lyβ/Lyα ratio, which is similar to that in the CIE scenario as a function of temperature (Figure 3). Therefore, the high O Lyβ/Lyα ratio cannot be explained in the NEI regime either.

4.2. Charge Exchange

The CX process involves an electron transferring from one atom or ion to another. Specifically, the CX relevant to X-ray astrophysics usually refers to a donor H/He atom colliding with a highly ionized ion (e.g., O^{+7}, O^{+8}). During the collision, an electron may be transferred from the atom to the ion, and recombined to a highly excited state, which will then cascade to the ground level and result in a series of emission lines in the X-ray spectrum. In the case of charge exchanged to a H-like O ion ($H + O^{+7} \rightarrow H^{+} + O^{+6}$), the emission of the recombined, excited O^{+6} ion is dominated by a bright O VII forbidden line, which will lead to a large G-ratio (e.g., R. K. Smith et al. 2012; L. Gu et al. 2016; L. Gu & C. Shah 2023).

At the outermost layer of an SNR, the upstream neutral atoms will pass through the shock front and interact with the downstream hot ions, which provides a promising site for CX to take place. Observational evidence of CX emission has been found in the optical band for many SNRs as the broad-line component in Balmer-dominated (nonradiative) shocks (e.g., Tycho, SN 1006, Cygnus Loop, RCW 86, SNR 0509-67.5; R. Kirshner et al. 1987; P. Ghavamian et al. 2001; E. A. Helder et al. 2010). However, in X-rays, there are only a few cases that have been indicated (e.g., Cygnus Loop, Puppis A, G296.1−0.5; S. Katsuda et al. 2011, 2012; S. R. Roberts & Q. D. Wang 2015; Y. Tanaka et al. 2022). Evidence of X-ray CX emission has been found in other (but relevant) astrophysical environments, such as at the interface between old overlapping SNRs and molecular clouds (e.g., in the Carina and 30 Doradus star-forming complexes; L. K. Townsley et al. 2011b, 2011a, 2024). We then explored whether CX may help to explain the observed line ratios in SN 1987A.

We added a CX component (described by the `vacx2` model in PyXSPEC) to the DEM model adopted in L. Sun et al. (2025), in order to see whether it could improve the spectral fits. We fixed the collision velocity as 500 km s^{-1}, while leaving the plasma temperature and normalization free to vary. We fitted the SN 1987A spectra in all epochs with this model including CX emission. However, we only found considerable improvement in the C statistics in one observation (observation ID 0556350101 taken in 2009 January), for which we got $\Delta C = -13.5$ with $\Delta\mathrm{dof} = -2$. For other observations, this model provides no significant improvements to the fitting ($\overline{\Delta C} \sim -1.8$ with $\Delta\mathrm{dof} = -2$). The CX emission may arise from plasmas with different collision velocities and temperatures. We have investigated this effect by changing the collision velocity from 50 to 1000 km s^{-1} and by adding another `vacx2` component with different temperatures, while the resulting C statistics show little changes.

The major problem of the CX scenario is that it cannot explain the enhanced Lyβ/Lyα ratio, i.e., the suppressed Lyα flux. On the contrary, the O VIII Lyα line should also be boosted by CX, as long as there are enough O^{+8} ions. In order to quantify the effects of CX emission on Lyβ/Lyα, we calculated the O VIII Lyα and Lyβ fluxes and derived the line ratios under the CX scenario. We explored a large parameter space, where the plasma temperature varies in the range of 0.1–10 keV and the collision velocity varies in the range of 50–1000 km s^{-1}. We found that the O VIII Lyβ/Lyα ratio mainly depends on the collision velocity, where the line ratio decreases from ∼0.128 to ∼0.098 with the collision velocity increasing from 50 to 1000 km s^{-1}. Given a certain collision velocity, the line ratio shows no significant variation with the varying temperature. Assuming a contribution of CX emission as high as 50% to the total O VIII emission, it will slightly increase the line ratio at low temperatures while slightly decreasing the line ratio at high temperatures (as seen in the right panel of Figure 3). However, in general, the expected Lyβ/Lyα ratio is still $\lesssim$0.15 and thus cannot explain the observations.

4.3. Resonant Scattering

In modeling the X-ray emission of SNRs, it is commonly assumed that the plasmas are optically thin. However, this may not be the case under certain conditions, especially for the emission from resonance lines. The photon emitted from a

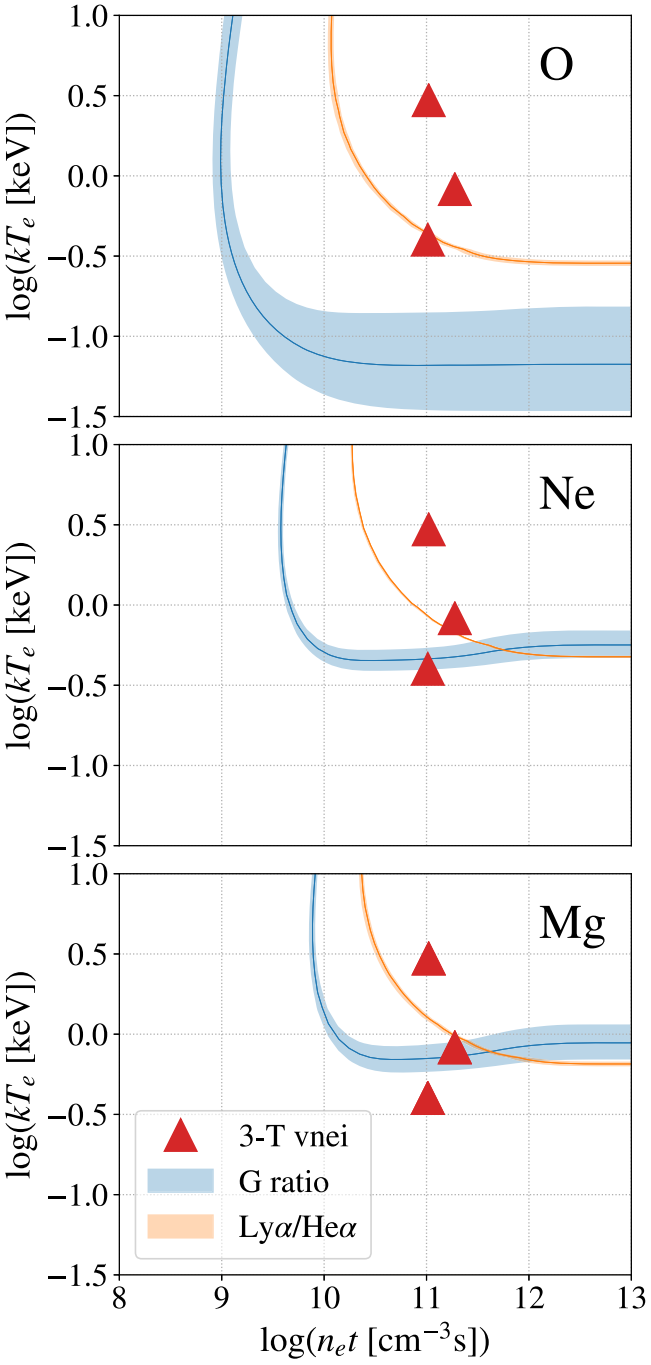

Figure 4. kT_e and n_et parameter spaces confined by the observed G-ratios and Lyα/Heα ratios of O, Ne, and Mg for SN 1987A. The 3-T `vnei` results are adopted from E. Greco et al. (2022).

resonant (allowed) transition can be efficiently (characterized by a larger cross section than forbidden transitions) absorbed by a suitable ion through resonant absorption. And for a resonant absorption from $n = 1$ to $n = 2$, the excited state will decay immediately by emitting a photon with roughly the same energy, but in a random direction. Therefore, the resonant absorption happening within the source is often referred to as "resonant scattering," since there is usually no reduction in the number of resonance line photons. If the optical depth is large enough (either due to a large length scale or a high density of the source), RS may become significant and alter the resonance line flux and its surface brightness distribution.

In X-rays, RS effects have been mostly studied in the diffuse hot plasma of elliptical galaxies, galaxy clusters, and galactic bulges (e.g., H. Xu et al. 2002; Y. Chen et al. 2018; Hitomi Collaboration et al. 2018; P. Chakraborty et al. 2023), for which RS-modified line fluxes and surface brightness distributions have been used to infer the turbulent Mach numbers. As for SNRs, there have been a few indications of the presence of RS effects, including the enhanced O VII G-ratios observed in DEM L71 (K. J. van der Heyden et al. 2003), the Cygnus Loop (H. Uchida et al. 2019), and N49 (Y. Amano et al. 2020). Despite the small size of SN 1987A, its rather high density ($\sim$2400 cm^{-3} for the shocked ER; L. Sun et al. 2021) still make it possible for the RS effects to be significant. Here, we first make a rough estimation of the RS optical depths of the O VII resonance line and O VIII Lyα line in SN 1987A (RS has little effect on the O VII forbidden and intercombination lines and O VIII Lyβ, given their small oscillator strengths, i.e., $\sim 2.0 \times 10^{-10}$, $\sim 8.2 \times 10^{-5}$, and $\sim 3.9 \times 10^{-2}$, respectively).

The optical depth of the resonant absorption (scattering) at the line centroid can be evaluated as (J. S. Kaastra & R. Mewe 1995)

$$\tau = \frac{4.24 \times 10^6 f\, N_{\rm H,20} \left(\frac{n_{\rm i}}{n_{\rm Z}}\right)\left(\frac{n_{\rm Z}}{n_{\rm H}}\right)\left(\frac{M}{T_{\rm keV}}\right)^{\frac{1}{2}}}{E_{\rm eV}\left(1 + \frac{0.0522 M \nu_{100}^2}{T_{\rm keV}}\right)^{\frac{1}{2}}}, \quad (1)$$

where f is the oscillator strength of the line, $N_{\rm H,20}$ is the hydrogen column density in units of 10^{20} cm^{-2}, $n_{\rm i}$ is the ion density, $n_{\rm Z}$ is the density of the element, $n_{\rm H}$ is the hydrogen density, M is the atomic weight of the ion, $T_{\rm keV}$ is the ion temperature in keV, $E_{\rm eV}$ is the line centroid energy in eV, and ν_{100} is the microturbulence velocity in units of 100 km s^{-1}. Adopting a distance to SN 1987A of 51.4 kpc (N. Panagia 2005), an angular size of $\sim 2''$ (e.g., J. L. Racusin et al. 2009), a hydrogen density of $\sim$2400 cm^{-3} (L. Sun et al. 2021), an O abundance of $\sim$0.18 solar abundance (e.g., L. Sun et al. 2021; E. Greco et al. 2022), a turbulence velocity of $\sim$500 km^{-1} (evaluated from the measured O VII line width by R. Sturm et al. 2010), and a He-like O ion fraction of $\sim$0.14 (taking $kT_{\rm e} = 0.4$ keV and $n_{\rm e}t = 10^{11}$ cm^{-3} s; e.g., E. Greco et al. 2022), we got an estimation of the O VII resonance line optical depth as $\tau_{\rm O\ VII} \sim 2.4$ and the O VIII Lyα optical depth as $\tau_{\rm O\ VIII} \sim 2.2$.[9] Given the fact that the shocked gas in SN 1987A spans a large range of physical properties, and considering the uncertainties in previous studies, we then estimated a range of the optical depths. For plasma with temperatures in the range of 0.3–1 keV and ionization parameters in the range of 10^{11}–10^{12} cm^{-3} s (which may be the major plasma component that contributes to O line emission), we got the optical depth of the O VII resonance line in the range of $\sim$0.01–5, with an emissivity-weighted average value of $\sim$2.7, and the optical depth of O VIII Lyα in the range of $\sim$0.01–2.3, with an emissivity-weighted average value of $\sim$1.3.

[9] Here, we assumed the O ion temperature is equal to the electron temperature. It is possible that the ion temperature is much higher than the electron/proton temperature (e.g., M. Miceli et al. 2019). However, even if we take an O ion temperature as high as 20 times the electron temperature (i.e., $\sim$8 keV), we still got an optical depth $\sim$2. And in that case, the inferred microturbulence velocity will be much lower, since the observed line width will be more attributed by thermal broadening.

However, a large optical depth of RS does not necessarily lead to the change of observed resonance line flux. It highly depends on the geometry of the hot gas distributed in the remnant and in what perspective we observe it. For example, if we observe the resonance line emission from the whole region of a spherically symmetric SNR, the RS will not make any difference to the integral line flux. However, the surface brightness distribution of the line may be modified, and the line flux from a certain subregion of the remnant can be changed. As shown by Y. Li et al. (2024) using Monte Carlo (MC) simulations, for a spherically symmetric SNR with a Sedov–Taylor gas distribution, if the optical depth is large enough, the resonance line flux will be significantly suppressed at the outer dense shell, but will be enhanced at the inner low-density region of the remnant. On the other hand, an SNR with highly asymmetric geometry, just like SN 1987A, may exhibit abnormal resonance line flux due to RS effects, even if we observe the integral spectrum from the whole remnant.

For a better understanding of the possible impact that RS may have on the observed line flux, we performed an MC simulation on the RS processes of O VII resonance line emission in SN 1987A. The fundamental physics of RS and the MC algorithm adopted in our simulation follow Y. Chen et al. (2018) and Y. Li et al. (2024). We assumed a ring-like structure for SN 1987A, picturing the dense ER. As demonstrated in Figure 5, the geometry of the ring is characterized by an inner radius $R_{\rm i}$, an outer radius $R_{\rm s}$, and a height h. The inclination angle θ is defined as the angle between the ER plane and the line of sight. Given the average radius of the ER as $\sim 0\farcs8$ and the average half-width as $\sim 0\farcs22$ (e.g., J. L. Racusin et al. 2009), we adopted $R_{\rm i}$ $\sim 0\farcs58$ and $R_{\rm s}$ $\sim 1\farcs02$, and assumed the ring height as equal to its width, thereby h $\sim 0\farcs44$. Other parameters (including hydrogen density, O abundance, turbulence velocity, temperature, and ionization parameter) were set the same as above.

The MC simulation shows that the maximum optical depth of the O VII resonance line along the line of sight, as a function of the inclination angle, can reach $\sim$1.7 when $\theta = 0^\circ$ (edge on) and $\sim$0.4 when $\theta = 90^\circ$ (face on). That means the photon initially going along the equatorial plane will have a greater chance of being scattered. Thereby, the line flux will be suppressed along the equatorial plane, while it will be enhanced in polar directions. As a result, the observed G-ratio can be changed due to RS, depending on the inclination angle—enhanced by a factor of $\sim$1.13 at $\theta = 0^\circ$ while being suppressed by a factor of $\sim$0.95 at $\theta = 90^\circ$ (Figure 5). Given the inclination angle of the ER as $\theta \sim 47^\circ$ (B. E. K. Sugerman et al. 2005), the simulation results indicate that the O VII G-ratio will be marginally suppressed by a factor of $\sim$0.96. Therefore, the observed enhancement of the G-ratio is unlikely to be caused by RS effects.

Similar inferences also work for O VIII Lyα line flux and the resulting Lyβ/Lyα ratio. Despite the absolute values being different, the O VIII Lyα line flux will also be suppressed along the equatorial plane while being enhanced in polar directions under the assumption of a ring-like geometry of SN 1987A, just like that for the O VII resonance line. At the inclination angle of SN 1987A, we will expect a marginally enhanced O VIII Lyα flux, which will result in a marginally suppressed rather than enhanced O VIII Lyβ/Lyα ratio (RS has little effect on O VIII Lyβ due to its small oscillator strength, as mentioned above). Therefore, the observed enhancement of the O VIII Lyβ/Lyα ratio is also unlikely to be due to RS effects.

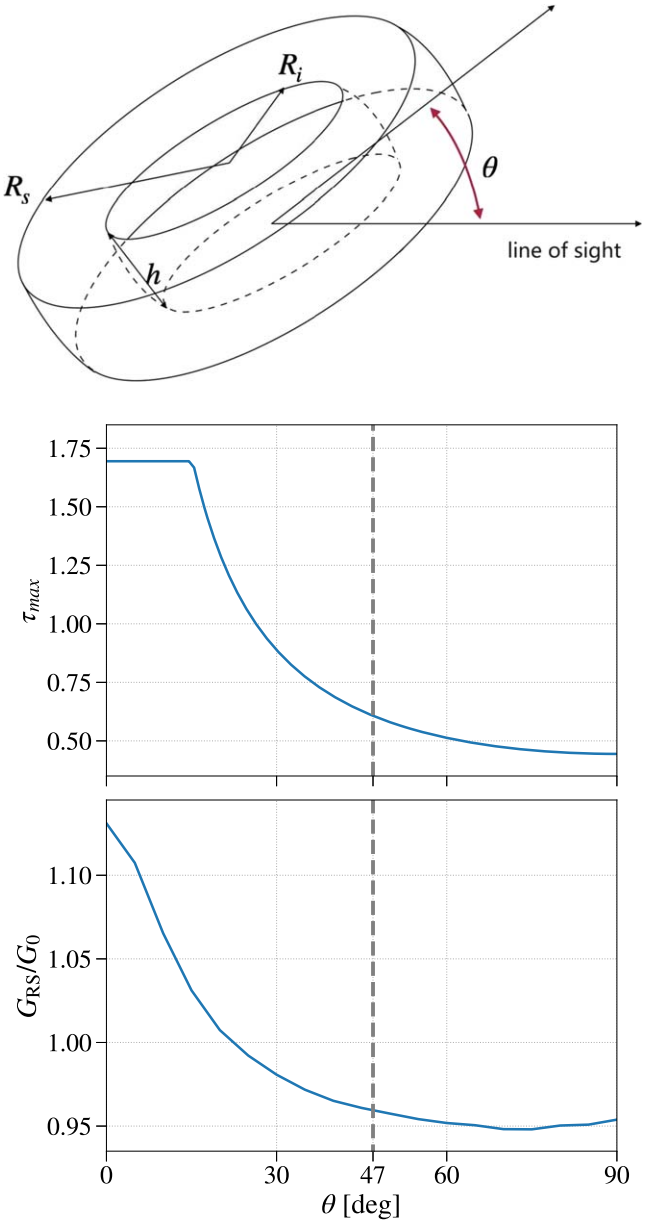

Figure 5. Top: geometry setup adopted for the MC simulation of the RS effect in SN 1987A. Middle: maximum RS optical depth as a function of the inclination angle. Bottom: RS-modified G-ratio, relative to the value without RS, as a function of inclination angle. The gray dashed line denotes the inclination angle for the ER of SN 1987A ($\sim$47°).

4.4. Absorption of Foreground Hot Gas

The X-ray emission of SN 1987A may be subject to absorption from the hot, ionized foreground gas, which has not been considered by the `tbvarabs` model adopted in the DEM analysis in L. Sun et al. (2025). We note that the underlying physical mechanism here is actually the same as that in RS. As described in Section 4.3, during the RS process, a photon is initially absorbed by an appropriate ion and then promptly reemitted in a random direction with roughly the same energy. However, when RS occurs along the line of sight but outside the emitting source, the effect of scattering is approximately

Table 2
Gaussian Absorption Fitting Result

Obs. Date	Age (Days)	$\tau_{\rm O\ VII}$	$\tau_{\rm O\ VIII}$	ΔC	ΔAIC	F-test p-value	Significance[a]
2007 Jan 17	7267	$0.76^{+0.75}_{-0.49}$	0.18 ± 0.03	−37.8	−29.8	2.5×10^{-6}	$\gtrsim 4.5\sigma$
2008 Jan 11	7627	$0.48^{+2.27}_{-0.30}$	0.21 ± 0.02	−49.4	−41.4	7.9×10^{-9}	$>5\sigma$
2009 Jan 30	8012	0.53 ± 0.16	$0.18^{+0.17}_{-0.10}$	−23.3	−15.3	6.5×10^{-4}	$\gtrsim 3.5\sigma$
2009 Dec 11	8327	0.47 ± 0.14	0.20 ± 0.02	−72.4	−64.4	1.1×10^{-11}	$>5\sigma$
2010 Dec 12	8693	0.43 ± 0.22	0.20 ± 0.03	−48.3	−40.3	2.0×10^{-8}	$>5\sigma$
2011 Dec 2	9048	0.71 ± 0.29	0.08 ± 0.03	−17.84	−9.8	7.6×10^{-3}	$\gtrsim 2.5\sigma$
2012 Dec 11	9423	0.76 ± 0.19	0 (<0.11)	−10.8	−6.8	1.1×10^{-2}	$\gtrsim 2.5\sigma$
2014 Nov 29	10141	0.32 (<0.75)	$0.18^{+0.18}_{-0.10}$	−4.7	+3.3	0.45	···
2015 Nov 15	10492	0.74 ± 0.53	0 (<0.04)	−11.9	−5.9	2.6×10^{-2}	$\gtrsim 2\sigma$
2016 Nov 2	10845	0.49 ± 0.22	0 (<0.13)	−0.3	+3.7	0.91	···
2017 Oct 15	11192	0.76 (<1.47)	$0.39^{+0.27}_{-0.23}$	−13.1	−5.1	3.7×10^{-2}	$\gtrsim 2\sigma$
2019 Nov 27	11964	0.73 (<1.22)	0.05 (<0.28)	−1.2	+2.8	0.60	···
2020 Nov 24	12328	0 (<0.83)	$0.36^{+0.19}_{-0.14}$	−8.9	−0.9	0.11	$\gtrsim 1.5\sigma$
2021 Dec 28	12727	0 (<1.16)	0.11 (<0.18)	−12.1	−6.1	2.5×10^{-2}	$\gtrsim 2\sigma$

Notes.
[a] Approximated from the F-test p-value, only for those with ΔAIC < 0.

equivalent to absorption. To differentiate from the RS process occurring within the source, as discussed in Section 4.3, we simply refer to it as "absorption" in this paper.

The resonant absorption of the O VII and O VIII resonance lines may lead to high G-ratios and high Lyβ/Lyα ratios. Such hot gas has been observed and constrained in the Galactic halo from both emission (e.g., D. B. Henley & R. L. Shelton 2013; M. Ueda et al. 2022; G. Ponti et al. 2023) and absorption (e.g., Q. D. Wang et al. 2005; Y. Yao et al. 2008; Y. Luo et al. 2018) perspectives. Additionally, the hot phase ISM in the LMC (e.g., S. L. Snowden & R. Petre 1994; M. Sasaki et al. 2002) may also contribute to the absorption column density.

We examined the absorption scenario by adding two Gaussian absorption components (`gabs`) to the DEM model adopted in L. Sun et al. (2025). We fixed the absorption line centroids (0.5739 keV for the O VII Heα resonance line and 0.6535 keV for O VIII Lyα line) while leaving the line widths σ and the absorption strengths ω free to vary (then the optical depth at the line center is given by $\tau = \frac{\omega}{2\pi\sigma}$).[10] We found considerable improvement in the C statistics ($\Delta C < -10$) for 10 observations out of 14 after introducing the Gaussian absorption components. Particularly, for the first five observations (taken from 2007 to 2011, when the O lines were around their maximum fluxes), we got $\Delta C < -20$. The obtained optical depths and the ΔC are listed in Table 2.

In order to better evaluate and demonstrate the significance of the added Gaussian absorption components, we further looked into the Akaike information criterion (AIC; H. Akaike 1974) values and performed an F-test for each observation. The AIC is commonly used as a robust criterion to select the best model that fits to data, where the model with a lower AIC value is preferred. The AIC value can be calculated as

$$\mathrm{AIC} = 2k - 2\ln L = 2k + C, \tag{2}$$

where k is the number of free parameters, and L is the likelihood of the model. In our case, a negative ΔAIC suggests that the model with absorption lines offers a better fit to the data. As listed in Table 2, we obtained ΔAIC < 0 for 11 out of 14 observations. Especially, all seven observations taken in 2007–2012 (when the O lines were around their maximum luminosities) result in ΔAIC < 0, which prefers the hot gas absorption scenario. In addition to the AIC, we performed an F-test for each observation, and derived the p-value. We also approximated the corresponding sigma levels based on the p-values for reference. The F-test p-values, together with the approximated sigma levels, are also listed in Table 2. We obtained F-test p-values <0.05 for 10 of 14 observations, which may approximately correspond to $\gtrsim 2\sigma$ significance. For all seven observations taken in 2007–2012, we obtained p-values $\lesssim 0.01$. The F-test further strengthens the preference of the hot gas absorption scenario. Furthermore, since the spectral fitting and the uncertainty estimation were performed in a Markov Chain Monte Carlo (MCMC) approach (running by the XSPEC `chain` command, containing 100,000 effective steps sampling with 40 walkers; for more information on the MCMC simulation, please refer to L. Sun et al. 2025), we produced and examined the MCMC corner plots of each fit. Figure 6 provides an example of the corner plots, adopting the fit to the 2009 January observation. As seen from the corner plot (e.g., the one for the O VII resonance line), despite the large scatterings of the probability distribution functions (PDFs) of the absorption strength and the line width as well as the potential degeneracy between them, the resulting PDF of the optical depth has a relatively small scattering, indicating a best-fit value significantly larger than zero.

Based on the fitting results of these observations, we estimated the average optical depths as $\tau_{\rm O\ VII} \sim 0.6$ for the O VII Heα resonance line and $\tau_{\rm O\ VIII} \sim 0.2$ for the O VIII Lyα line. The resonant absorption optical depth is formulated as in Equation (1). Assuming the H-like and He-like O ions share the same ion temperature and turbulence velocity, the ion fraction ratio between H-like and He-like O, $f_{\rm i,O\ VIII}/f_{\rm i,O\ VII}$ ($f_{\rm i} \equiv n_{\rm i}/n_{\rm Z}$) can be evaluated as

$$\frac{f_{\rm i,O\ V\ III}}{f_{\rm i,O\ V\ II}} = \left(\frac{\tau_{\rm O\ V\ III}}{\tau_{\rm O\ V\ II}}\right)\left(\frac{E_{\rm O\ V\ III}}{E_{\rm O\ V\ II}}\right)\left(\frac{f_{\rm O\ V\ III}}{f_{\rm O\ V\ II}}\right)^{-1}. \tag{3}$$

[10] The optical depth of the foreground hot gas is not expected to be different between different observations. However, since the X-ray flux of SN 1987A keeps changing, we are unable to fix the absorption strength at the same value for all the observations.

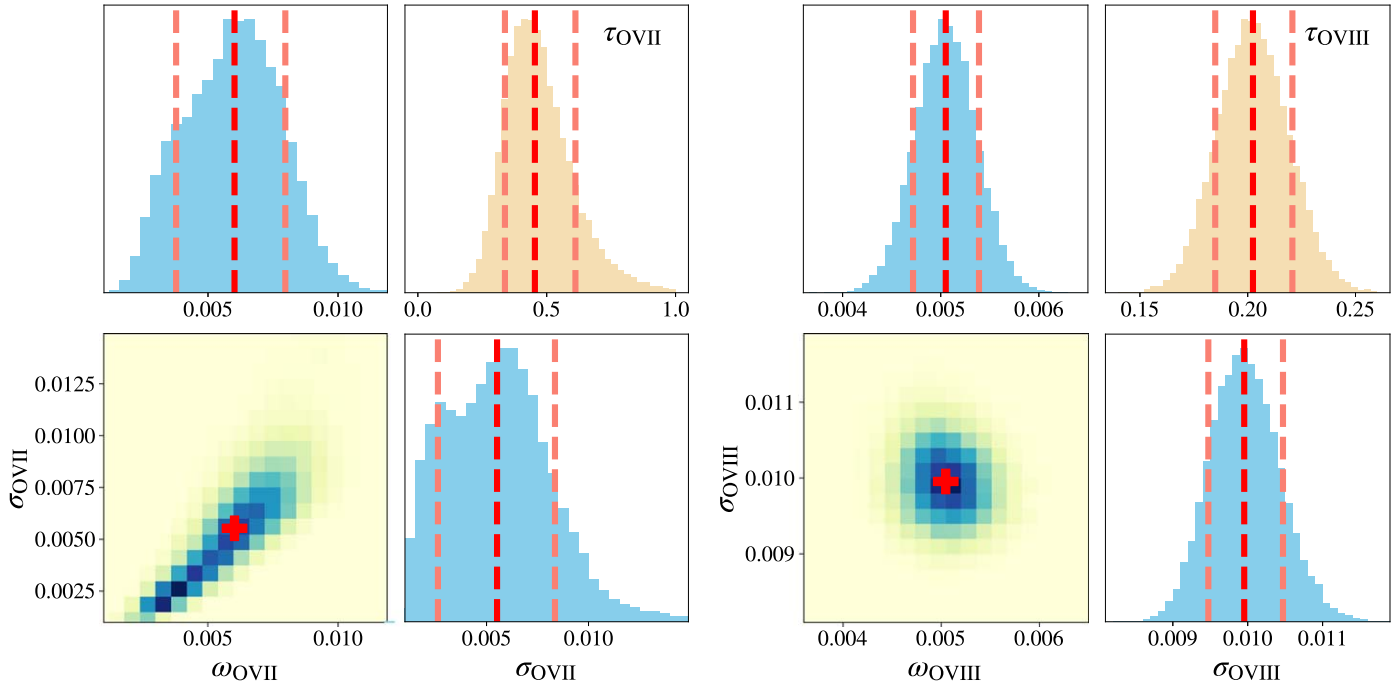

Figure 6. An example of the MCMC corner plots for the two Gaussian absorption components (O VII resonance line on the left and O VIII Lyα on the right, adopted from the fit to the 2009 January observation). The top-left and bottom-right panels show the PDFs of the absorption strength and the line width, respectively. The bottom-left panel shows their two-dimensional PDFs. The top-right panel shows the PDF of the derived optical depth. The red dashed lines and red crosses denote the best-fit values, while the pink dashed lines denote the 1σ errors.

Taking the oscillator strengths of the O Heα resonance line and Lyα line as $f_{\rm O\ VII} = 0.72$ and $f_{\rm O\ VIII} = 0.42$,[11] we got $f_{\rm i,O\ VIII}/f_{\rm i,O\ VII} \sim 0.65$. Assuming the hot gas is under the CIE state, the H-like/He-like O ion fraction ratio gives an electron temperature $kT_{\rm e} \sim 0.15$ keV. This temperature is consistent with the hot gas in the Galactic halo, for which other authors found a temperature $\sim$0.15–0.22 keV (e.g., D. B. Henley & R. L. Shelton 2013; M. Ueda et al. 2022; G. Ponti et al. 2023). Assuming the ion temperature is equal to the electron temperature and a turbulence velocity of 100 km s^{-1}, we further estimated the column density of the oxygen based on Equation (1) as $N_{\rm O} \sim 0.5 \times 10^{16}$ cm^{-2}. The oxygen column density we found is comparable with those suggested by previous studies on Galactic halo X-ray absorption lines ($\sim 10^{15}$–10^{16} cm^{-2}; e.g., Q. D. Wang et al. 2005; Y. Yao et al. 2008; Y. Luo et al. 2018).

Neglecting foreground hot gas absorption in previous studies led to an underestimation of the O VII resonance line and O VIII Lyα line fluxes, and thus an overestimation of the intrinsic O VII G-ratios and O VIII Lyβ/Lyα ratios. By incorporating the best-fit Gaussian absorption line components into the "`nla-pec + Gauss`" model, as described in Section 3, we measured the hot gas absorption-corrected O line fluxes. The intrinsic G-ratios and Lyβ/Lyα ratios were then calculated and are listed in Table 3. For most of the observations (especially those with significant absorption line detections), we obtained corrected O VII G-ratios in the range of 0.5–0.8 and corrected O VIII Lyβ/Lyα ratios in the range of 0.15–0.20. An intrinsic O VII G-ratio $\sim$0.5–0.8 is consistent with the expectation of NEI plasma with a temperature of $\sim$0.3–1 keV and an ionization parameter of 10^{11}–10^{12} cm^{-3} s, as seen in Section 4.1 and Figure 3. On the other hand, an intrinsic O VIII Lyβ/Lyα ratio of $\sim$0.15–0.20 seems to be still higher than what we expect for NEI/CIE plasma. However, considering a potential contribution of Fe XVIII F6 as (on average) $\sim$25% to the measured Lyβ flux (see the discussions in Section 3), the real Lyβ/Lyα ratio could also be consistent with the NEI/CIE plasma interpretation. Given the fact that the physical parameters (e.g., temperature and ionization parameter) of the hot plasma in SN 1987A keep varying, the intrinsic O line fluxes and ratios are expected to vary as well. Specifically, as shown in Figure 3, the intrinsic O VII G-ratio is expected to be decreasing, while O VIII Lyβ/Lyα is expected to be increasing with an increasing average temperature. Also, we note that the potential contribution of Fe XVIII F6 emission to the measured O VIII Lyβ flux, and thus the measured Lyβ/Lyα ratio, is expected to be increasing with increasing temperature. However, due to the large uncertainties, we could not address a significant time evolution trend of the measured intrinsic line ratios.

Neglecting foreground hot gas absorption also led to an underestimation of the O abundance in previous studies. For the observations taken in 2007–2010 (with $\gtrsim 3\sigma$ detection of the absorption components), the original DEM model gives O abundances ranging from $\sim$0.17–0.45, with an average value of $\sim$0.29 (L. Sun et al. 2025). After incorporating the absorption components, the obtained best-fit O abundances show an average increase of $\sim$20%, ranging from $\sim$0.22–0.53 with an average value of $\sim$0.34. On the other hand, the N/O ratio (by number of atoms) in this case is $\sim$1.2, which is consistent with the values obtained from optical studies (e.g.,

[11] The oscillator strengths of the two O Lyα lines are 0.28 for Lyα_1 ($2p^2P_{3/2} \rightarrow 1s^2S_{1/2}$) and 0.14 for Ly$\alpha_2$ ($2p^2P_{1/2} \rightarrow 1s^2S_{1/2}$). Given the Ly$\alpha_1$ and Lyα_2 lines are rather close in energy, they are not absorbed separately – photons from Lyα_1 or Lyα_2 can be absorbed by either line. Therefore, we take the sum of their oscillator strengths.

Table 3
Hot Gas Absorption-corrected Line Ratios and O Abundances

Obs. Date	Age (Days)	G-ratio[a]	Lyβ/Lyα[a]	O[b] (This Work)	O[b] (L. Sun et al. 2025)
2007 Jan 17	7267	$0.53^{+0.13}_{-0.12}$	0.16 ± 0.02	0.219 ± 0.010	$0.177^{+0.016}_{-0.010}$
2008 Jan 11	7627	0.67 ± 0.15	0.15 ± 0.01	0.328 ± 0.014	0.249 ± 0.017
2009 Jan 30	8012	0.77 ± 0.15	0.18 ± 0.01	$0.279^{+0.011}_{-0.012}$	$0.238^{+0.022}_{-0.010}$
2009 Dec 11	8327	0.61 ± 0.14	0.18 ± 0.02	0.343 ± 0.012	$0.324^{+0.048}_{-0.011}$
2010 Dec 12	8693	$0.63^{+0.17}_{-0.14}$	0.18 ± 0.02	0.538 ± 0.022	$0.450^{+0.087}_{-0.012}$
2011 Dec 2	9048	0.71 ± 0.17	0.21 ± 0.02	0.343 ± 0.015	$0.283^{+0.024}_{-0.023}$
2012 Dec 11	9423	$0.64^{+0.18}_{-0.17}$	0.23 ± 0.02	0.383 ± 0.010	$0.368^{+0.079}_{-0.025}$
2014 Nov 29	10141	0.79 ± 0.22	0.19 ± 0.02	0.440 ± 0.022	$0.373^{+0.041}_{-0.033}$
2015 Nov 15	10492	0.57 ± 0.25	0.20 ± 0.03	0.269 ± 0.007	$0.336^{+0.071}_{-0.024}$
2016 Nov 2	10845	$0.47^{+0.22}_{-0.17}$	0.21 ± 0.03	0.253 ± 0.010	$0.239^{+0.20}_{-0.29}$
2017 Oct 15	11192	0.69 ± 0.26	0.20 ± 0.02	$0.255^{+0.18}_{-0.17}$	$0.190^{+0.029}_{-0.013}$
2019 Nov 27	11964	0.76(<1.55)	0.26 ± 0.06	$0.406^{+0.041}_{-0.025}$	$0.396^{+0.138}_{-0.023}$
2020 Nov 24	12328	$0.29^{+0.27}_{-0.22}$	0.15 ± 0.03	0.350 ± 0.020	$0.268^{+0.041}_{-0.014}$
2021 Dec 28	12727	0.76(<1.64)	0.18 ± 0.04	$0.189^{+0.013}_{-0.008}$	$0.182^{+0.033}_{-0.012}$

Notes.
[a] Hot gas absorption-corrected (i.e., intrinsic) line ratios.
[b] O abundance in units of solar abundance (J. Wilms et al. 2000).

~1.1–1.5; P. Lundqvist & C. Fransson 1996; S. Mattila et al. 2010).

5. Conclusion

In this work, we took a further look into the residuals left in the DEM modeling of SN 1987A by L. Sun et al. (2025), focusing on the O lines. We revised and updated the O line fluxes on the basis of L. Sun et al. (2021). We found a high O VII G-ratio $\gtrsim$1 and a high O VIII Lyβ/Lyα ratio $\gtrsim$0.2 in SN 1987A. In order to explore their physical origin, we performed a detailed investigation into four possible scenarios, i.e., NEI effects, CX, RS, and hot gas absorption. Neither NEI, CX, or RS can fully explain the observed O line ratios, while the spectral fitting can be considerably improved by adding two Gaussian absorption components at the O VII resonance line and O VIII Lyα line. We obtained the optical depths as $\tau_{\rm O\ VII} \sim 0.6$ for the O VII resonance line and $\tau_{\rm O\ VIII} \sim 0.2$ for the O VIII Lyα line. The estimated temperature ($kT_{\rm e} \sim 0.15$ keV) and column density ($N_{\rm O} \sim 0.5 \times 10^{16}$ cm^{-2}) of the absorbing gas is consistent with the hot Galactic X-ray halo. We suggest, therefore, that the high G-ratio and Lyβ/Lyα ratio in SN 1987A are most likely caused by the absorption of the foreground hot gas. The O abundance of SN 1987A might be underestimated in previous studies due to neglecting the foreground hot gas absorption. We found an average increase of ~20% in the best-fit O abundances after adding the absorption components, which leads to an N/O ratio ~1.2 (by number of atoms).

However, we note that, while hot gas absorption is likely playing the major role, all the possible mechanisms mentioned above may simultaneously contribute to the modification of the line ratios. We also note that a few LMC SNRs have already been found to exhibit unusual O line ratios, such as DEM L71 (K. J. van der Heyden et al. 2003), N49 (Y. Amano et al. 2020), N132D (H. Suzuki et al. 2020), and J0453.6−6829 (Y. Koshiba et al. 2022). Even though for most of them the abnormal line ratios have been attributed to CX or RS effects, the absorption of the hot Galactic halo gas may contribute as well. In the near future, spatially resolved high-resolution X-ray spectroscopic studies with, e.g., XRISM, HUBS, and the Line Emission Mapper, may help to better constrain the contributions of CX, RS, and hot gas absorption in these remnants.

Acknowledgments

L.S. and Y.C. acknowledge NSFC funding under grant Nos. 12173018, 12121003, and 12393852. L.S. acknowledges support from the Jiangsu Funding Program for Excellent Postdoctoral Talent (grant No. 2023ZB252). P.Z. thanks the support from NSFC grant No. 12273010. S.O., E.G., and M.M. acknowledge financial contributions from the PRIN 2022 (20224MNC5A) – "Life, death and after-death of massive stars" funded by the European Union – Next Generation EU, and the INAF Theory Grant "Supernova remnants as probes for the structure and mass-loss history of the progenitor systems." We are grateful for valuable suggestions from John Raymond.

Software: XSPEC (K. A. Arnaud 1996), SPEX (J. S. Kaastra et al. 1996), SAS (C. Gabriel et al. 2004).

ORCID iDs

Lei Sun https://orcid.org/0000-0001-9671-905X
Salvatore Orlando https://orcid.org/0000-0003-2836-540X
Emanuele Greco https://orcid.org/0000-0001-5792-0690
Marco Miceli https://orcid.org/0000-0003-0876-8391
Yiping Li https://orcid.org/0000-0001-7571-2318
Yang Chen https://orcid.org/0000-0002-4753-2798
Jacco Vink https://orcid.org/0000-0002-4708-4219
Ping Zhou https://orcid.org/0000-0002-5683-822X

References

Akaike, H. 1974, ITAC, 19, 716
Alp, D., Larsson, J., & Fransson, C. 2021, ApJ, 916, 76
Amano, Y., Uchida, H., Tanaka, T., Gu, L., & Tsuru, T. G. 2020, ApJ, 897, 12
Arnaud, K. A. 1996, in ASP Conf. Ser. 101, Astronomical Data Analysis Software and Systems V, ed. G. H. Jacoby & J. Barnes (San Francisco, CA: ASP), 17
Bray, E., Burrows, D. N., Park, S., & Ravi, A. P. 2020, ApJ, 899, 21

Brown, G. V., Beiersdorfer, P., Liedahl, D. A., Widmann, K., & Kahn, S. M. 1998, ApJ, 502, 1015
Burrows, D. N., Michael, E., Hwang, U., et al. 2000, ApJL, 543, L149
Chakraborty, P., Foster, A., Smith, R., Brickhouse, N., & Raymond, J. 2023, ApJ, 959, 126
Chen, Y., Wang, Q. D., Zhang, G.-Y., Zhang, S., & Ji, L. 2018, ApJ, 861, 138
Dewey, D., Dwarkadas, V. V., Haberl, F., Sturm, R., & Canizares, C. R. 2012, ApJ, 752, 103
Frank, K. A., Zhekov, S. A., Park, S., et al. 2016, ApJ, 829, 40
Gabriel, C., Denby, M., Fyfe, D. J., et al. 2004, in ASP Conf. Ser. 314, Astronomical Data Analysis Software and Systems (ADASS) XIII, ed. F. Ochsenbein, M. G. Allen, & D. Egret (San Francisco, CA: ASP), 759
Ghavamian, P., Raymond, J., Smith, R. C., & Hartigan, P. 2001, ApJ, 547, 995
Greco, E., Miceli, M., Orlando, S., et al. 2021, ApJL, 908, L45
Greco, E., Miceli, M., Orlando, S., et al. 2022, ApJ, 931, 132
Gu, L., Kaastra, J., & Raassen, A. J. J. 2016, A&A, 588, A52
Gu, L., & Shah, C. 2023, arXiv:2301.11335
Haberl, F., Geppert, U., Aschenbach, B., & Hasinger, G. 2006, A&A, 460, 811
Helder, E. A., Broos, P. S., Dewey, D., et al. 2013, ApJ, 764, 11
Helder, E. A., Kosenko, D., & Vink, J. 2010, ApJL, 719, L140
Heng, K., Haberl, F., Aschenbach, B., & Hasinger, G. 2008, ApJ, 676, 361
Henley, D. B., & Shelton, R. L. 2013, ApJ, 773, 92
Hitomi Collaboration, Aharonian, F., Akamatsu, H., et al. 2018, PASJ, 70, 10
Kaastra, J. S., & Bleeker, J. A. M. 2016, A&A, 587, A151
Kaastra, J. S., & Mewe, R. 1995, A&A, 302, L13
Kaastra, J. S., Mewe, R., & Nieuwenhuijzen, H. 1996, in 11th Colloquium on UV and X-ray Spectroscopy of Astrophysical and Laboratory Plasmas, ed. K. Yamashita & T. Watanabe (Tokyo: Universal Academy Press), 411
Kaastra, J. S., Paerels, F. B. S., Durret, F., Schindler, S., & Richter, P. 2008, SSRv, 134, 155
Katsuda, S. 2023, arXiv:2302.13775
Katsuda, S., Tsunemi, H., Mori, K., et al. 2011, ApJ, 730, 24
Katsuda, S., Tsunemi, H., Mori, K., et al. 2012, ApJ, 756, 49
Kirshner, R., Winkler, P. F., & Chevalier, R. A. 1987, ApJL, 315, L135
Koshiba, Y., Uchida, H., Tanaka, T., et al. 2022, PASJ, 74, 757
Lawrence, S. S., Sugerman, B. E., Bouchet, P., et al. 2000, ApJL, 537, L123
Li, Y., Zhang, G.-Y., Chen, Y., Sun, L., & Zhang, S. 2024, ApJ, 967, 99
Lundqvist, P., & Fransson, C. 1996, ApJ, 464, 924
Luo, Y., Fang, T., & Ma, R. 2018, ApJS, 235, 28
Maitra, C., Haberl, F., Sasaki, M., et al. 2022, A&A, 661, A30
Mattila, S., Lundqvist, P., Gröningsson, P., et al. 2010, ApJ, 717, 1140
Mewe, R. 1999, in X-Ray Spectroscopy in Astrophysics, ed. J. van Paradijs & J. A. M. Bleeker, Vol. 520 (Berlin: Springer), 109
Miceli, M., Bocchino, F., Decourchelle, A., Ballet, J., & Reale, F. 2010, A&A, 514, L2
Miceli, M., Orlando, S., Burrows, D. N., et al. 2019, NatAs, 3, 236
Orlando, S., Ono, M., Nagataki, S., et al. 2020, A&A, 636, A22
Panagia, N. 2005, in IAU Colloq. 192, Cosmic Explosions, On the 10th Anniversary of SN 1993J, ed. J.-M. Marcaide & K. W. Weiler (Berlin: Springer), 585
Park, S., Burrows, D. N., Garmire, G. P., et al. 2002, ApJ, 567, 314
Park, S., Zhekov, S. A., Burrows, D. N., Garmire, G. P., & McCray, R. 2004, ApJ, 610, 275
Park, S., Zhekov, S. A., Burrows, D. N., & McCray, R. 2005, ApJL, 634, L73
Park, S., Zhekov, S. A., Burrows, D. N., et al. 2006, ApJ, 646, 1001
Ponti, G., Zheng, X., Locatelli, N., et al. 2023, A&A, 674, A195
Porquet, D., Dubau, J., & Grosso, N. 2010, SSRv, 157, 103
Racusin, J. L., Park, S., Zhekov, S., et al. 2009, ApJ, 703, 1752
Ravi, A. P., Park, S., Zhekov, S. A., et al. 2021, ApJ, 922, 140
Ravi, A. P., Park, S., Zhekov, S. A., et al. 2024, ApJ, 966, 147
Roberts, S. R., & Wang, Q. D. 2015, MNRAS, 449, 1340
Sasaki, M., Haberl, F., & Pietsch, W. 2002, A&A, 392, 103
Smith, R. K., Foster, A. R., & Brickhouse, N. S. 2012, AN, 333, 301
Snowden, S. L., & Petre, R. 1994, ApJL, 436, L123
Sonneborn, G., Pun, C. S. J., Kimble, R. A., et al. 1998, ApJL, 492, L139
Sturm, R., Haberl, F., Aschenbach, B., & Hasinger, G. 2010, A&A, 515, A5
Sugerman, B. E. K., Crotts, A. P. S., Kunkel, W. E., Heathcote, S. R., & Lawrence, S. S. 2005, ApJS, 159, 60
Sun, L., Vink, J., Chen, Y., et al. 2021, ApJ, 916, 41
Sun, L., Orlando, S., Greco, E., et al. 2025, ApJ, in press
Suzuki, H., Yamaguchi, H., Ishida, M., et al. 2020, ApJ, 900, 39
Tanaka, Y., Uchida, H., Tanaka, T., et al. 2022, ApJ, 933, 101
Townsley, L. K., Broos, P. S., Chu, Y.-H., et al. 2011a, ApJS, 194, 16
Townsley, L. K., Broos, P. S., Chu, Y.-H., et al. 2011b, ApJS, 194, 15
Townsley, L. K., Broos, P. S., & Povich, M. S. 2024, ApJS, 273, 5
Uchida, H., Katsuda, S., Tsunemi, H., et al. 2019, ApJ, 871, 234
Ueda, M., Sugiyama, H., Kobayashi, S. B., et al. 2022, PASJ, 74, 1396
van der Heyden, K. J., Bleeker, J. A. M., Kaastra, J. S., & Vink, J. 2003, A&A, 406, 141
Wang, Q. D., Yao, Y., Tripp, T. M., et al. 2005, ApJ, 635, 386
Wilms, J., Allen, A., & McCray, R. 2000, ApJ, 542, 914
Xu, H., Kahn, S. M., Peterson, J. R., et al. 2002, ApJ, 579, 600
Yao, Y., Nowak, M. A., Wang, Q. D., Schulz, N. S., & Canizares, C. R. 2008, ApJL, 672, L21
Zhekov, S. A., McCray, R., Borkowski, K. J., Burrows, D. N., & Park, S. 2006, ApJ, 645, 293
Zhekov, S. A., McCray, R., Dewey, D., et al. 2009, ApJ, 692, 1190
Zhekov, S. A., Park, S., McCray, R., Racusin, J. L., & Burrows, D. N. 2010, MNRAS, 407, 1157